JWSR

3D Numerical Simulation of the Separated Turbulent Shallow Flow around a Single Side Obstacle

A. Safarzadeh[1*], L. Esfandiary[2]

1. Department of Civil Engineering, University of Mohaghegh Ardabili, Ardabil, Iran

2. Department of Civil Engineering, K.N Toosi University of Technology, Tehran, Iran

ABSTRACT

In this paper, the performance of Reynolds Averaged Navier Stokes (RANS) simulations was evaluated to predict the flow structure developed by the presence of a sidewall obstruction in a uniform open-channel shallow flow. The study of these flow structures is important because they present in several real world configurations, such as groynes in rivers, where the erosion processes, mass transport, and influence of the flow hydrodynamics in ecological processes are still not well understood. Results of the numerical simulations were compared with the experimental laboratory measurements based on the Surface Particle Image Velocimetry (SPIV). It was found that the length of the main recirculation region obtained by two-equation models was 29% shorter than the measured one, while the predicted length by the Reynolds Stress Model (RSM) was in good agreement with the SPIV results. All of the performed RANS simulations were unable to predict properly the secondary separation region, which occurs immediately downstream of the side obstacle. This part of the flow field is a dead zone and due to extremely low velocity, the flow is laminar.

1. Introduction

Shallow flows are found in many ubiquitous natural flows such as wide rivers, coastal regions, even in the atmosphere. Jirka (2001) defines shallow flows as predominantly horizontal flows in a fluid domain for which the two horizontal dimensions greatly exceed the vertical one. Flow structures which arise from localized or distributed transverse disturbances may grow into large scale instabilities. These instabilities are characterized by a highly organized vortical motion, which is normally termed as quasi two dimensional coherent structures (2DCS). Jirka (2001) classifies 2DCS based on their generation mechanisms: Type "A" caused by topographic forcing, Type "B" due to internal transverse shear instabilities and Type "C" produced by secondary instabilities of the vertically sheared base flow.

Type "A" is the most evident generation mechanism of 2DCS and typically occurs whenever topographical features generate a strong flow separation. Bridge abutment, single groyne and island are few examples of topographic forcing. Type "B" occurs where the transverse gradient of the velocity gives rise to flow instabilities and leads to the development of a mixing layer characterized by distinct vortices with vertical rotating axes. Many fluid domains of environmental engineering importance contain turbulent shallow mixing layers. Some typical examples can be found in stream confluences (Rhoads &

* Corresponding Author Email: Safarzadeh@uma.ac.ir

Sukhodolov, 2004, Uijttewaal and Booij, 2000) at the interface between groyne fields and main flow (Brevis, 2009), in harbor entrances and in shallow vegetated flows (White & Nepf, 2007).

One of the most interesting features of the shallow flow downstream a side obstacle is the occurrence of two different vortical flow generation mechanisms, a clear difference with the so called free mixing layer. Following Jirka (2001), the main two generation mechanism in this case are those due to topographical forcing and internal shear instabilities. Firstly, the obstacle presence induces a transverse contraction which breaks the horizontal symmetry of the approaching flow. Due to the resulting adverse pressure gradient, the main flow separates and generates a train of vortices directly from the obstacle head. Secondly, downstream of the obstacle, the separation gives rise to a main and secondary recirculation cells (Talstra et al., 2006). The lateral flow velocity difference between circulating regions and the main flow leads to the development of an intense shear region, which produces lateral shear instabilities, resulting in the generation of the shear layer vortex.

The interaction between the two types of vortices increases the complexity of the spatial and temporal structures of the mixing layer (Safarzadeh and Salehi, 2013). Furthermore, due to the flow shallowness, the bottom friction affects the development and spatial evolution of the generated horizontal large-scale structures.

Another interesting feature of the separated shallow flows is the presence of distinctly different length scales along the shear layer, at the vicinity of the side obstacle and at the rear of the separation region. Experimental observations and spectral analysis of the measured velocity time series conducted by

Safarzadeh and Salehi (2013) showed that the shear layer has both of three-dimensional and two dimensional characteristics. Figure 1 illustrates temporal flow structure down-stream of the side obstacle measured by SPIV.
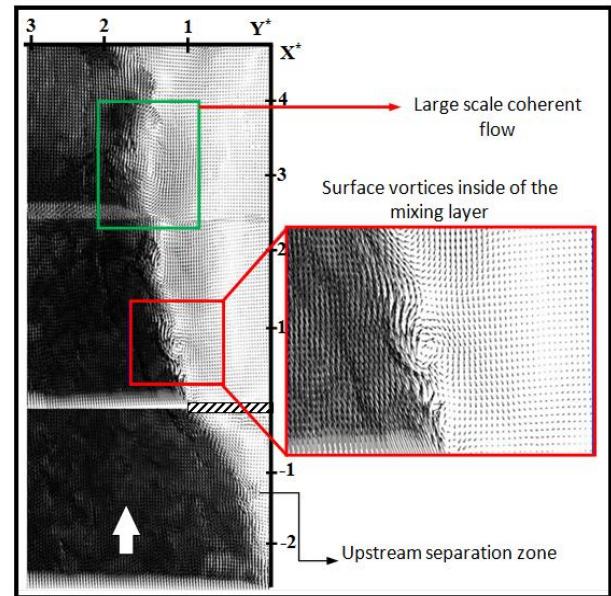
Fig.1.Temporal flow structure generated by side obstacle and obtained by SPIV Measurement (Safarzadeh and Salehi, 2013)

At the rear of the separation region, where the large scale 2DCS breaks and the bed generated turbulent flow is the dominant mechanism, spectral analysis showed that the energy spectrum at the higher frequencies follow the well-known Kolmogorov -5/3 power law, which confirms the flow three dimensionality. Following the downstream direction, the 2DCS length scale of the vortices populating the mixing layer becomes even larger than the length of the side obstacle. The -3 slope of the energy spectrum at the lower frequencies also confirms this statement. Consequently, analytical or comp-utational methods of separated shallow flows should be able to account for the effect of the aforementioned flow characteristics. Current-ly, several approaches exist for the simulate-on of the turbulent fluid flows. Direct

Numerical Simulations (DNS) have become a crucial tool to improve the understanding of fundamental turbulence phenomena such as intermittency (Ishihara et al., 2009) and the dynamic of near wall coherent structures (Adrian and Marusic, 2012). Due to the high computational cost of DNS simulations, they are normally constrained to small physical domains and relatively low Reynolds numbers. Advances have been made to develop eddy-resolving techniques such as Large Eddy Simulation (LES) and Detached Eddy Simulations (DES), however they still remain computationally prohibitive for practitioners requiring routine calculations of high Reynolds number flows such as those found in nature. Therefore, it is still necessary to evaluate the performance of statistically based RANS approaches to simulate the time-averaged characteristics of such flows. This work aims at assessing the performance of three RANS turbulent closures for the simulation of the flow developed by the presence of a lateral hydraulic structure in a shallow flow.

2. Test Case

Safarzadeh and Salehi (2013) conducted an experimental investigation on turbulent shallow flow around a single side obstacle. The experiment was conducted in a rectangular cross section tilting shallow flume with an effective length of Lt=18 m and a width of B=1.82 m located at the Institute for Hydromechanics (IfH), Karlsruhe Institute of Technology, Germany. Figure 2 illustrates the experimental set up. A single obstacle was used to apply the geometrical forcing to the approaching flow which results in the formation of a large separation region with an intense turbulent shear layer bounding the separation region. The outline of the single obstacle was chosen to be a rectangular element of 0.25 m×0.05 m×0.05 m length, height

and width, respectively. The inclination angle of the side obstacle was 90° to the main flow and it was emerged during the measurement.

The origin of the coordinate axis was located at the downstream face of the side obstacle at the junction point with the side wall. $X*$ and $Y*$ are dimensionless stream wise and transverse axes, respectively that are defined as $X*=X/L$ and $Y*=Y/L$. Where, L is the length of the side obstacle. Table 1 summarizes the experimental conditions. The width to depth ratio maintains shallow flow conditions and the selected Reynolds and Froude numbers, based on flow depth and bulk mean velocity, and ensured a turbulent and sub-critical flow. In this table, I is the longitudinal slope of the channel in degree, $C_f=2\tau_b/\rho U_0^2$ is the bed friction coefficient where τ_b is the bed shear stress, Q_{in} and U_0 are discharge and Bulk velocity at the inlet of the channel, respectively. The following formula recommended by the ASCE Task Force on friction factor in open channel flow (1963) was used to calculate C_f:

$$\frac{1}{\sqrt{c_f}} = -4\log\left(\frac{k_s}{12H} + \frac{1.25}{\text{Re}\sqrt{c_f}}\right) \qquad (1)$$

In the above expression, k_s is the equivalent sand-grain roughness which is related to the diameter of the bed sand diameter (d) as three times the sand particles diameter (Jirka, 2001). H is the water depth and Re and Fr are Reynolds and Froude numbers, respectively. The bed friction number, $S=cfB/2H$ was 0.66 and the flow falls in shallow condition as suggested by Babarutsi et al. (1989) for $S>0.1$. Surface Particle Image Velocimetery (SPIV) used to measure the instantaneous turbulent flow field generated by the side obstacle. The measurements were conducted by two synchronized CCD cameras with 37 Hz acquisition frequency. Long term measurements were performed and the mean

field and horizontal components of the Reynolds stress tensor were calculated. This information was used to evaluate the performance of the RANS models. In the following section, a brief description of the numerical simulation is presented.

Table 1. Experimental conditions of the test case (Safarzadeh and Slehi, 2013)

Parameter	Value
Q_{in} [lit/s]	13.5
H [cm]	4
I [degree]	0.01
U_0 [cm/s]	18
B/H [-]	46
Re [-]	29680
Fr [-]	0.29
C_f [-]	0.072
S [-]	0.66

3. Numerical Simulation

3.1. Mean Flow Equations

For an incompressible fluid flow, the equation of continuity and balance of momentum for the mean motion, in Cartesian coordinates are given as follows (Celik, 1999):

$$\frac{\partial U_i}{\partial x_i} = 0 \tag{2}$$

$$U_j \frac{\partial U_i}{\partial x_j} = -\frac{\partial P}{\partial x_i} + gx_i + \mu \frac{\partial^2 U_i}{\partial x_i x_j} + \frac{\partial R_{ij}}{\partial x_j} \tag{3}$$

where U_i is time averaged velocity in I direction, x_i is the position vector, P is the mean pressure and μ is the dynamic viscosity. $R_{ij} = -\rho \overline{u_i' u_j'}$ is the Reynolds stress tensor. Here $u_i = u_i' + U_i$, where u_i, u_i' and U_i are total, fluctuating and time averaged fluid velocity components, respectively. In two equation model, the Reynolds stress is modeled using Boussinesq's assumption (Celik, 1999):

$$-\rho \overline{u_i' u_j'} = 2\mu_t S_{ij} - \frac{2}{3}\rho k \delta_{ij} \tag{4}$$

where μ_t is the eddy viscosity, S_{ij} and k are mean strain rate tensor and turbulent kinetic energy, respectively that are defined as follows (Celik, 1999):

$$S_{ij} = \frac{1}{2}\left(\frac{\partial U_i}{\partial x_j} + \frac{\partial U_j}{\partial x_i}\right) \tag{5}$$

$$k = \frac{1}{2}\left(\overline{u_i' u_j'}\right) \tag{6}$$

δ_{ij} is the Kronecker delta. Reynolds stresses are modeled using various available turbulence models. A brief description of the different turbulence models used in the current research will be given in the following section.
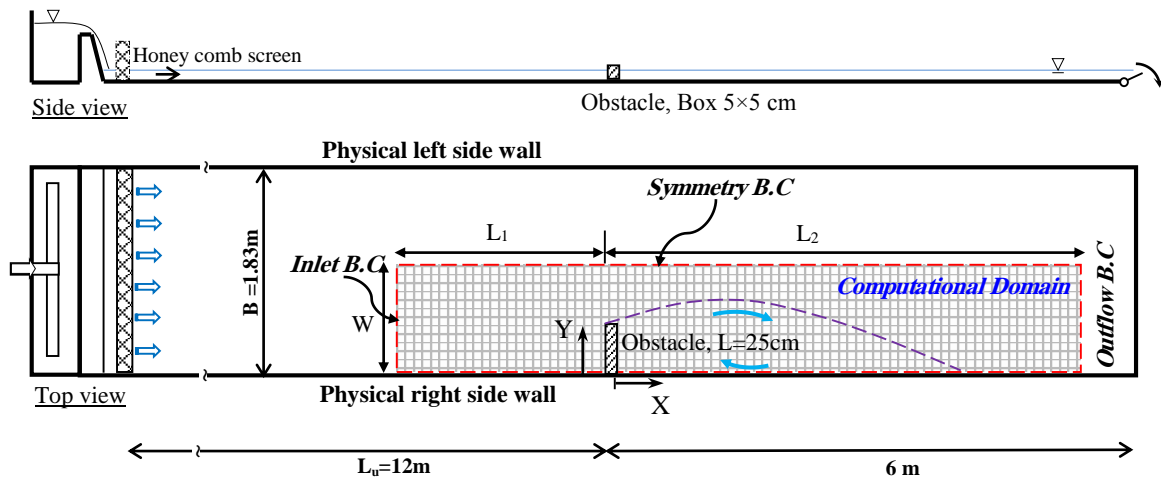
Fig. 2. Geometrical specifications of the test case (Safarzadeh and Salehi, 2013). The area denoted by red dashed lines shows the computational domain in the present numerical simulation.

3.2. Turbulence Closure Equations

Turbulent stresses in Reynolds-averaged equations can be estimated using any of the several existing turbulence models. No single turbulence model is accepted universally for solving all classes of problems, but each model has certain advantages.

3.2.1 Standard κ-ε Turbulence Model

The simplest and most widely used two-equation turbulence model is the k-ε model, which solves two separate transport equations to allow the turbulent kinetic energy, k, and its dissipation rate, ε, to be independently determined. According to this model, the eddy viscosity is related to the turbulence kinetic energy (k) and its rate of dissipation (ε) (Launder & Spalding, 1972):

$$\mu_t = \rho \, C_\mu \frac{k^2}{\varepsilon} \qquad (7)$$

The turbulence quantities k and ε are calculated by following transport equations:

$$U_i \frac{\partial k}{\partial x_i} = \frac{\partial}{\partial x_i}\left(\frac{\mu_t}{\rho \delta_k}\frac{\partial k}{\partial x_i}\right) + \frac{\mu_t}{\rho} \times$$
$$\left(\frac{\partial U_i}{\partial x_j} + \frac{\partial U_j}{\partial x_i}\right)\frac{\partial U_i}{\partial x_j} - \varepsilon \qquad (8)$$

$$U_i \frac{\partial \varepsilon}{\partial x_i} = \frac{\partial}{\partial x_i}\left(\frac{\mu_t}{\rho \delta_\varepsilon}\frac{\partial \varepsilon}{\partial x_i}\right) + c_{\varepsilon 1}\frac{\varepsilon}{k}G$$
$$-c_{\varepsilon 2}\frac{\varepsilon^2}{k} \qquad (9)$$

where G is the turbulence production by mean shear modeled as follows:

$$G = \frac{\mu_t}{\rho}\left(\frac{\partial U_i}{\partial x_j} + \frac{\partial U_j}{\partial x_i}\right)\frac{\partial U_i}{\partial x_j} \qquad (10)$$

Closure coefficients used in this model are summarized in Celik (1999).

3.2.2 Standard k-ω Turbulence Model

Another two-equation model available in most of the CFD codes is the k-ω model, which was introduced by Wilcox (1994). In contrast to the k-ε model that solves for the dissipation (ε) or the rate at which the turbulent kinetic energy (k) is transformed, the k-ω model solves the rate at which the dissipation occurs (the turbulent frequency, ω). Dimensionally, ω can be related to ε by $\omega = \varepsilon/k$, and the eddy viscosity is computed as (Wilcox, 1994):

$$\mu_t = \rho \frac{k}{\omega} \qquad (11)$$

The turbulence quantities k and ω are calculated by following transport equations:

$$\rho \frac{\partial k}{\partial x_i} = \frac{\partial}{\partial x_i}\left[(\mu + \frac{\mu_t}{\delta_\omega})\frac{\partial k}{\partial x_i}\right] + \tau_{ij}\frac{\partial u_i}{\partial x_j}$$
$$-\beta^* \rho k \omega \qquad (12)$$

$$\rho \frac{\partial \omega}{\partial x_i} = \frac{\partial}{\partial x_i}\left[(\mu + \frac{\mu_t}{\delta_\omega})\frac{\partial \omega}{\partial x_i}\right] + \alpha\frac{\omega}{k}\tau_{ij}\frac{\partial u_i}{\partial x_j}$$
$$-\beta \rho \omega^2 \qquad (13)$$

where τ_{ij} is the stress tensor and defined as follows:

$$\tau_{ij} = \left[(\mu + \mu_t)\left(\frac{\partial U_i}{\partial x_j} + \frac{\partial U_j}{\partial x_i}\right)\right] -$$
$$\left[\frac{2}{3}\left(\frac{k}{\rho} + \mu_t\right)\frac{\partial U_i}{\partial x_i}\delta_{ij}\right] \qquad (14)$$

Closure coefficients used at this model are summarized in Celik (1999).

3.2.3 RSM Turbulence Model

The Reynolds stress model (RSM) solves the Reynolds-averaged Navier-Stokes equations by using the Reynolds stresses transport equations (seven-equations for 3D flow) and an equation for the dissipation rate, ε. The RSM accounts for the effects of the streamline curvature, vorticity, circulation,

and rapid changes in the strain rate in a more efficient way than the two-equation models. However, it requires more computational effort and time. The transport equation in this model is as follows (Launder, 1989, a and b):

$$
\frac{\partial}{\partial t}(\rho \overline{u_i' u_j'}) + \frac{\partial}{\partial x_k}(\rho u_k \overline{u_i' u_j'}) =
$$

$$
\frac{\partial}{\partial x_k}\left[(\rho \overline{u_i' u_j' u_k'}) + \overline{p(\delta_{kj} u_i' + \delta_{ik} u_j')} \right] +
$$

$$
\frac{\partial}{\partial x_k}\left[\mu \frac{\partial}{\partial x_k}(\overline{u_i' u_j'}) \right] -
$$

$$
\rho\left(\overline{u_i' u_k'}\frac{\partial u_j}{\partial x_k} + \overline{u_j' u_k'}\frac{\partial u_i}{\partial x_k} \right) +
$$

$$
\overline{p(\frac{\partial u_i'}{\partial x_j} + \frac{\partial u_j'}{\partial x_i})} - 2\mu(\overline{\frac{\partial u_i'}{\partial x_k}\frac{\partial u_j'}{\partial x_k}})
$$

$$
-2\rho\ \Omega_k (\overline{u_j' u_m'}\varepsilon_{ikm} + \overline{u_i' u_m'}\varepsilon_{jkm})
$$

(15)

Left hand side terms are the local time derivatives and convection term (C_{ij}), respectively. Terms of the right hand side are turbulent diffusion ($D_{T,ij}$), molecular diffusion ($D_{L,ij}$), stress production (P_{ij}), pressure strain (ϕ_{ij}), dissipation (ε_{ij}) and production by system rotation (F_{ij}), respectively. Most of the terms in the above transport equation includeing C_{ij}, $D_{L,ij}$ and P_{ij} do not require any modeling and are directly solved. However, $D_{T,ij}$ (Lien and Leschziner, 1994), ϕ_{ij} and ε_{ij} (Gibson and Launder, 1978; Launder, 1989a and b) need to be modeled to close the transport equation. To simulation the pressure strain (ϕ_{ij}), the linear pressure-strain method is used.

3.3. Numerical Solution

Fluent 6.4 was used to simulate the flow field. This code uses the Finite-Volume (FVM) discretization method in conjunction with different turbulence models. Different schemes such as Upwind, SOU, Power Law and Quick may be used to discretize the convection terms of the transport equations.

Pressure and velocity field coupling may be done by SIMPLE, SIMPLEC or PISO algorithms. Flow geometry and computational mesh were generated using Gambit software.

4. Model Set up and Computational Details

In Fig. 2, the computational domain is superimposed to the experimental layout. Various numerical simulations were conducted to find the appropriate domain size (to find the optimum values of the L_1, L_2 and W), optimum grid spacing and also to find the appropriate turbulence model. As it is depicted in Fig. 2, the simulation domain is extended up to L_1 upstream of the side obstacle and the inlet velocity boundary condition implemented at the upstream boundary of the simulation domain. The velocity field and turbulence parameters (k, ε and ω) are imposed from a separate simulation of the fully developed turbulent flow through a straight channel. It was found that the $(L_1)_{min} = 10L$ is enough to ensure that the side obstacle does not affect the inlet boundary. At the downstream end of the model, the outflow boundary condition was used. This condition states that the gradients of all variables (except pressure) are zero in the flow direction. At this boundary, the flow often reaches a fully developed state. To ensure that this condition was satisfied at the exit of the simulation domain (a fully developed separation eddy forms), it was found that the optimum value of $(L_2)_{min} = 25L$.

Wall boundary condition was implemented to the right side boundary of the simulation domain, while to minimize the computational time, the left side boundary was simulated as a symmetrical boundary condition and various simulations were conducted to find the optimum value for W. It was found that $W = 5L$ is the optimum value to ensure that the left side symmetry boundary is not affected

by the presence of the side obstacle. Experimental measurements revealed that due to the flow shallowness, variations of the flow depth around the side obstacle is less than 10% of the maximum water depth in the flow field (Safarzadeh and Salehi, 2013). Regarding the notes reported by Rodi and Leschzeiner (1981), the upper boundary was specified as symmetry condition, which enforces a rigid lid with zero normal velocity and a zero shear stress. At the solid boundaries (Channel bed and periphery of the side obstacle), the wall boundary condition was used. Considering the bed roughness and bulk velocity of the inlet flow, walls were hydraulically smooth and the no-slip and no-flux conditions were imposed. The implementation of wall boundary conditions in turbulent flows starts with the evaluation of:

$$y^+ = \frac{\Delta y_p}{\nu} \sqrt{\frac{\tau_w}{\rho}} \qquad (16)$$

where Δy_p is the distance of the near-wall node to the solid surface and τ_w is the wall shear stress. The distance of the first grid surface off the walls is important and depends on the flow conditions, wall roughness and the turbulence model that is used. The k-ε model uses the wall function to bridge the solution variables at the near-wall cells and the corresponding quantities on the wall. However, the k-ω model resolves the near wall region (laminar sub layer region). The firs grid surface of the solid boundaries was at $\Delta y_p=0.0001$ m, which ensures that the first grid surface off the wall is located almost everywhere at $y^+=1.0$ and that at least two grid surfaces are located within the laminar sublayer ($y^+<5.0$).

Non-uniform mesh was used close to the solid boundaries, since it is refined close to the side obstacle and along the shear layer, where both of the mean and turbulent flows have strong gradients in all directions. Figure

3 shows the computational mesh for the case with lateral extension of the domain *W=7.3L*, or the full width case. At each case, the sensitivity analysis was used to find the optimum number of the computational meshes. For example, for the case which is illustrated in Fig. 3, it was found that simulation with a total number of 1550346 cells resulted in an accurate flow field and increasing cells number to over two times, had no significant change in the results. Due to existence of circulation and separation regions in the flow field, convection terms were discretized using the second order upwind (SOU) scheme (Patankar, 1980). Staggered mesh in conjunction with PISO algorithm was used for the flow field solution.
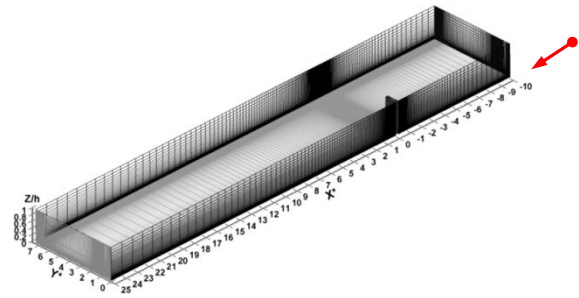
Fig. 3. Computational mesh for W=7.3L case

The convergence criterion was set to 10^{-5} for residuals of all of the governing equations and in order to ensure the real convergence of the numerical simulation, velocity magnitude of some points was monitored during solution process to reach a converged value. Simulations were performed in parallel processing mode using a 16 core Xeon server with 24 Giga-byte of Ram.

5. Results and discussion

5.1. Model validation

Figure 4 shows the 2D streamlines in the water surface for the experimental measurements and numerical results. The experimental streamlines show a separation region just upstream of the obstacle and two recirculation

regions downstream, the primary (DP) and secondary (DS) recirculation flows, respectively. The time-mean length of the primary separation region (DP gyre), which is defined by the reattachment length and the streamwise extent of the second gyre were $L_m=11L$ and $L_s=3.2L$, respectively. The length of the secondary eddy was about one quarter the length of the main recirculation region and it was in close agreement with the results reported by previous research (Nassiri et al., 2002). Comparison of the experimental streamlines with numerical results showed that the length of the main recirculation region obtained by two-equation models was shorter than the measured one. The k-ω model performed better than the k-ε turbulence model.

The predicted length by RSM model was in good agreement with the SPIV results. The lack of precision of the 2-equation models in the regions of anisotropic turbulence, such as the separation region, is their main weakness. This is mainly due to the assumptions of the local equilibrium and local isotropy of the eddy viscosity. In this regard, the RSM model seems to be more accurate due to the fact that this model accounts for the effects of the streamline curvature, vorticity, circulation, and rapid changes in the strain rate in a more efficient way.

Due to the flow shallowness, the streamwise momentum of the reversed flow in the DP gyre decreased toward upstream along the channel wall and at $X^*=3.2$, it broke away from the side wall because of the local streamwise adverse pressure gradient, which arises from the presence of the dead water region at the junction region between the downstream face of the obstacle and the side wall. In other words, the reversed flow does not flow completely into the obstacle and sidewall junction, as its own inertia prevents a rapid change in direction. Consequently, the

separated flow deflected towards the channel center and an oblique interface developed between DP and the low velocity junction fluid. This fluid exchanged momentum along the oblique interface of the main vortex, causing a counter wise rotation of the primary vortex. Another important parameter affecting the formation of the secondary eddy is the retarding effects of the bed friction on the reversed flow. The bed friction affects the full depth of the shallow flow and consequently, reversed flow loss a part of its momentum by friction (Uijtewaal and Booij, 2000). This is why the secondary eddy dose not form in the deeper flow case.

All of the performed RANS simulations were unable to predict properly the secondary eddy, just downstream of the side obstacle. It is obvious from Fig. 4 that, similar to the main eddy, the performance of the RSM model was better than the 2-equation models.

RANS models assume turbulent flow all over the computational domain, while experimental measurements showed that in spite of the presence of the strongly turbulent flow along the mixing layer, the dead region just downstream of the obstacle exhibits characteristics of the laminar flow (Safarzadeh and Salehi, 2013).

Figure 5 compares the experimental and RSM results of the streamwise velocity component. A good agreement between measured and predicted results can be observed. However, in $X^*=1$, $X^*=3$ and $X^*=5$ profiles, some discrepancies can be found. This region represents the mixing layer region bounding the shallow separation region. Experimental observations revealed that the separated shallow mixing layers are characterized by energetic large scale coherent flow structures. Large scale eddies are highly anisotropic and as a consequence, RANS models are unable to properly predict them, affecting at same time the accuracy of the

mean flow. By increasing the mixing layer distance ($X^*>8$), the large scale eddies are dissipated and small scale eddies become the dominant turbulent flow features. Consequently, experimental and numerical

streamwise velocity profiles for $X^*=8$ and $X^*=11$ agree well.

Experimental, SPIV (Safarzadeh and Salehi, 2013)

Numerical Streamlines

k-ε Turbulence Model

k-ω Turbulence Model

RSM Turbulence Model
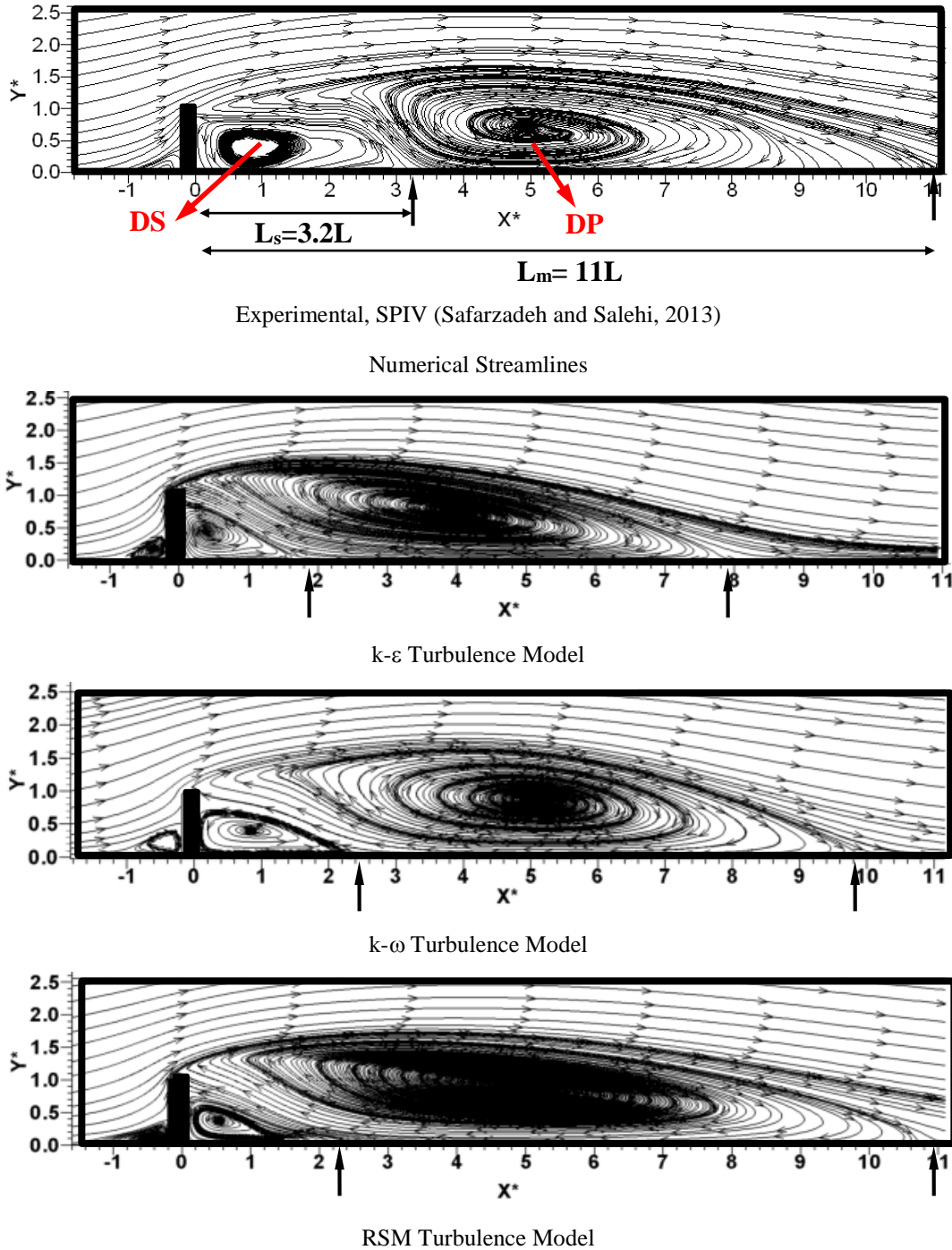
Fig. 4. Comparison of the stream line at water surface plane between SPIV measurement (Safarzadeh and Salehi, 2013) and numerical result with various turbulence models
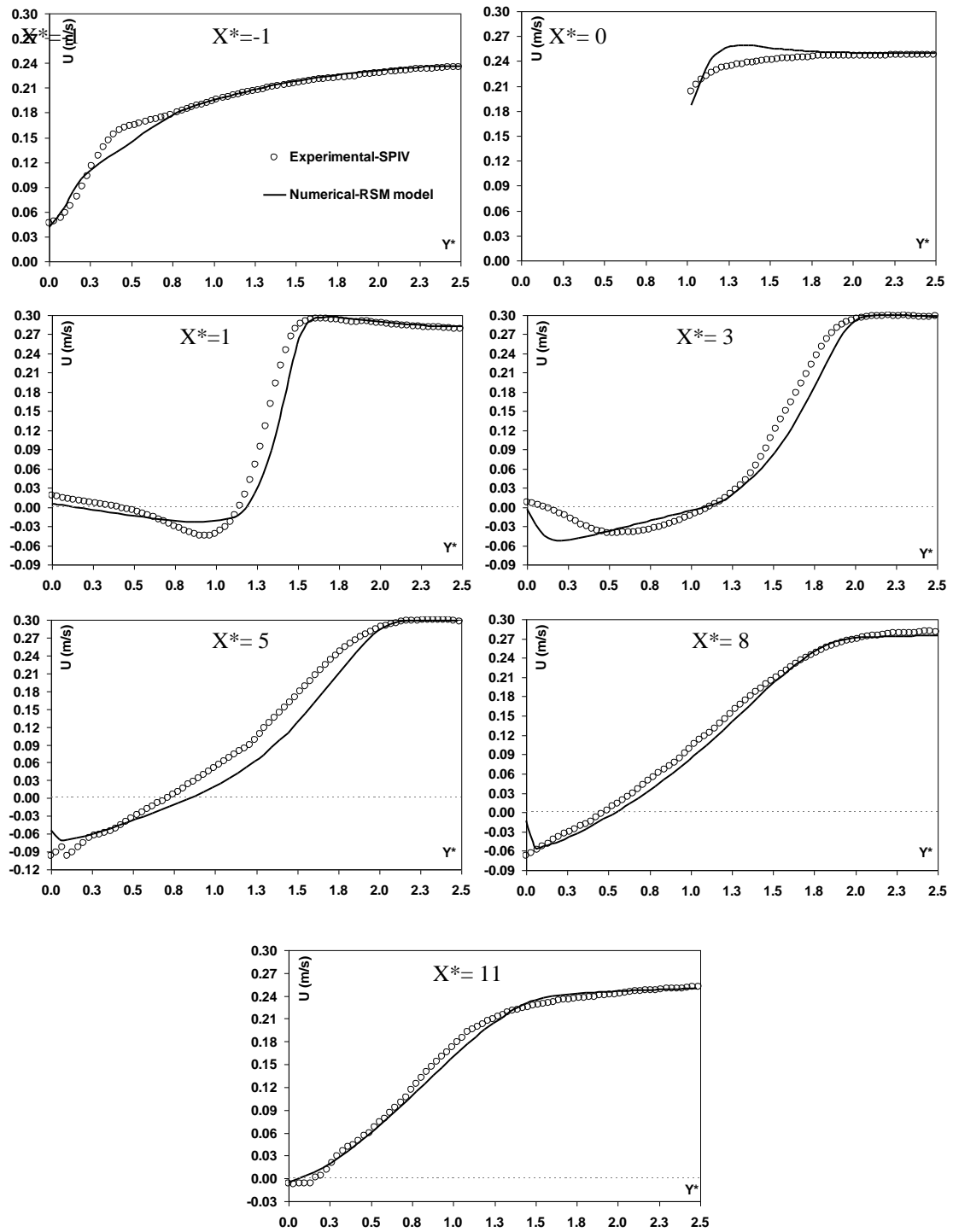
Fig. 5. Comparison of the transverse velocity profiles between SPIV measurements and numerical simulation using RSM turbulence model

5.2. Characteristics of the Mixing Layer

Figure 6 compares streamwise velocity contour plots between the measured and simulated results. Furthermore, inner and outer boundaries of the mixing layer are denoted by "+" and "×" symbols, respectively. Castro & Haque (1983) suggested the $\Delta y_H = (y_{0.95} - y_{0.67})$ and $\Delta y_L = (y_{0.67} - y_{0.2})$ as a measure to estimate the thickness of the mixing layer in high and low velocity sides, respectively. Where y_n is the point at which the velocity is $n\Delta U + U_{min}$. $\Delta U = U_{max} - U_{min}$ is the total streamwise velocity difference across the mixing layer at each transverse velocity profile. U_{max} and U_{min} are the maximum and minimum values of the streamwise velocity component, respectively.

The experimental results show an important change of the mixing layer width at X^*=3.2, while the numerical RSM model is unable to properly predict this phenomenon. This phenomenon is attributed to the unsteady turbulent nature of the reattachment region, the interaction of the primary and secondary gyres and their effects on generation and development of the large scale coherent structures at the intersection of two eddies (Safarzadeh and Salehi, 2013).

Figure 7 compares velocity vectors between measured and simulated cases using RSM turbulence model. It is clear that upstream of the side obstacle and in the accelerated zone at the outer side of the shear layer, velocity vectors coincide well in terms of both the magnitude and direction. At the interface zone of the main and secondary gyres and also at the reattachment zone, there were some discrepancies between the measured and simulated velocity vectors. The maximum deviation occurred at the interface zone, which is depicted by the dashed rectangle. This phenomenon clearly describes deficiency of the RANS models to simulate the interaction between the separation zones and consequently, the predicted mixing layer has a different shape than the measured one.

6. Conclusions

A commercially-available CFD code was used for prediction of the flow patterns generated by a side obstacle in a shallow flow. Three turbulence closure models were employ-ed and the performance of each model was evaluated using the experimental data. It was found that the length of the main recirculation region obtained by two-equation models is 20% shorter than the measured one, while the predicted length by RSM model was in good agreement with the SPIV results. All the performed RANS simulations were unable to predict properly the secondary separation region. Deficiency of RANS models were attributed to effects of large scale coherent flow structures through the mixing layer bounding the separation region downstream of the side obstacle. Comparison of the measured and predicted velocity vectors showed that the maximum deviation occurs at the interface zone between the main and secondary gyres.

Experimental (SPIV)

Numerical, RSM Turbulence Model
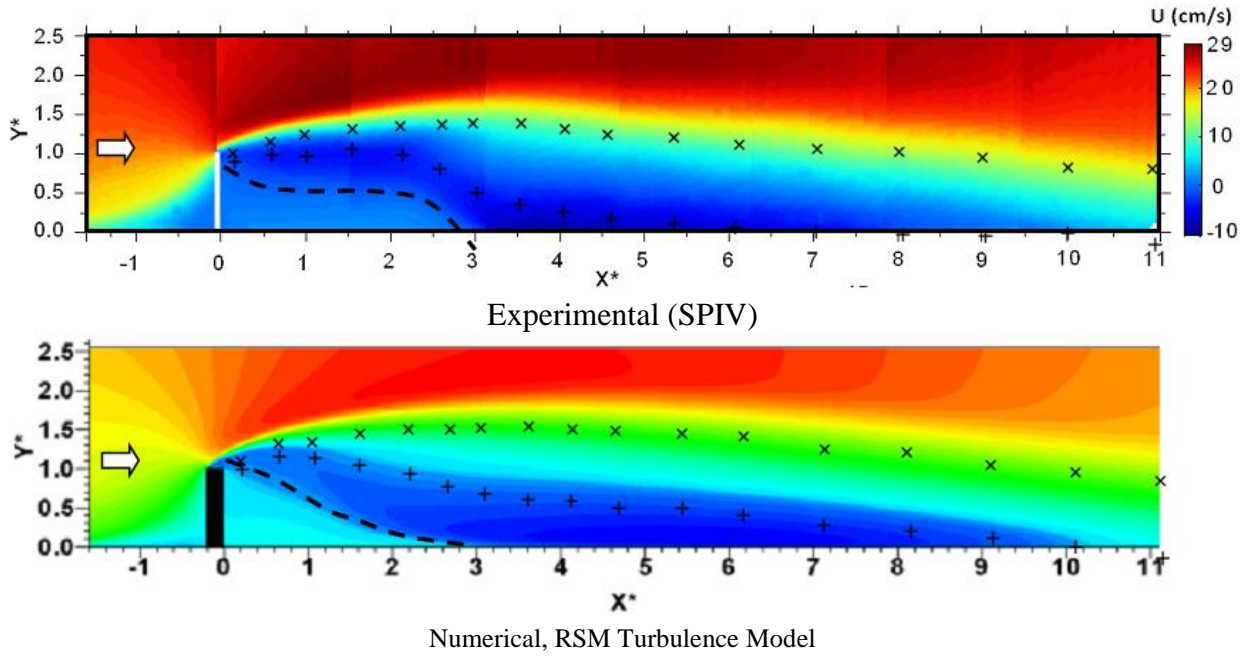
Fig. 6. Comparison of the stream wise velocity contours between SPIV measurements and numerical simulation using RSM turbulence model. "+" and "×" symbols denote inner and outer boundaries of the mixing layer, respectively
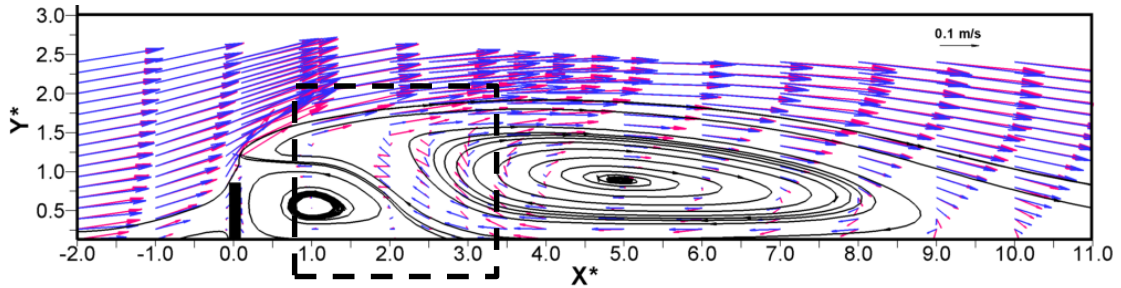
Fig.7. Comparison of the measured (Red) and RSM simulated (Blue) velocity vectors

NOMENCLATURE

X^*	dimensionless streamwise coordinate
Y^*	dimensionless transverse coordinate
τ_b	bed shear stress
U	approach bulk velocity
ρ	water density
c_f	bed friction coefficient
k_s	equivalent sand grain roughness
S	bed friction number
B	channel width

H	inlet water depth
I_0	channel slope
Re	Reynolds number
Fr	Froude number
Q_{in}	inlet discharge
u_i	velocity component
u_i'	fluctuating velocity component
U_i	mean velocity component
R_{ij}	Reynolds stress tensor
P	Pressure

34

μ	viscosity of fluid
μ_t	eddy viscosity
S_{ij}	strain rate tensor
K	turbulent kinetic energy
δ{ij}	Kronecker delta
ε	turbulence dissipation rate
δ_k	turbulent Prantdl number of k
δ_k	turbulent Prantdl number of ε
G	turbulence production by mean shear
ω	specific dissipation rate
τ_{ij}	stress tensor
C_{ij}	convection term
$D_{T,ij}$	turbulent diffusion
$D_{L,ij}$	molecular diffusion
P_{ij}	stress production
ϕ_{ij}	pressure strain
F_{ij}	Production by system rotation
Δy_p	distance of the near wall node

References

Adrian R. J., Marusic I., (2012), Coherent structures in flow over hydraulic engineering surfaces. J. Hydraul. Res., 50(5), 451-464.

Barbarutsi S., Ganoulis J., and Chu V.H., (1989), Experimental investigation of shallow recirculating flows. J. Hydraul. Eng. 128(10), 891-900.

Brevis W., (2009), Experimental investigation of the flow hydrodynamics in open channel dead regions. Ph.D. thesis, Universidad de Chile.

Castro I. P., and Haque A., (1987), The structure of a turbulent shear layer bounding a separation zone. J. Fluid Mech., 179(2), 439-468.

Celik I. B., (1999), Introductory Turbulence Modeling. Western Virginia University.

Gibson M. M. and Launder B. E., (1978), Ground effects on pressure fluctuations in the atmospheric boundary layer. J. Fluid Mech., 86,491-511.

Ishihara T., Gotoh T., Kaneda Y., (2009), Study of high-Reynolds number isotropic turbulence by direct numerical simulation. Ann. Rev. in Fluid Mech., 41, 165-180.

Jirka G. H., (2001), Large scale flow structures and mixing processes in shallow flows. J. Hydraul. Res., 39(6), 567-573.

Jirka G. H. and Seol D. G., (2010), Dynamics of isolated vortices in shallow flows.J. hydro- env. Res., 4(2), 65-73.

Launder B. E., (1989a), Second-moment closure and its use in modeling turbulent industrial flows. Int. J. of Num. Meth.in Fluids, 9, 963-985.

Launder B. E., (1989b), Secound-moment closure: present and future? Int. J. of Heat Fluid Flow, 10(4), 282-300.

Launder B. E., Spalding D. B., (1972), Lectures in Mathematical Models of Turbulence. Academia press, London, England.

Lien F. S. and Leschziner M. A., (1994), Assessment of turbulent transport models including non-linear RNG eddy-viscosity formulation and second-moment closure. Comp. and Fluids, 23(8), 983-1004.

Nassiri M., Chu V. H. and Babarutsi S., (2002), Simulation of horizontal turbulence in Shallow Recirculating Flows.Proceeding of 15th ASCE Engineering Mechanics Conference. June 2-5, 2002, Columbia University, New York, NY.

Rhoads B. L. and Sukhodolov A. N., (2004), Spatial and temporal structure of a shear layer turbulence at a stream confluence. Wat. Res. Res. 40, W06304, doi: 10.1029/2003WR002811.

Safarzadeh A., Salehi Neyshabouri, S. A. A., (2013), Hydrodynamics of the Mixing Layer Bounding a Separation Zone Using SPIV, Part1: Mean Flow Structure. Journal of Hydraulics, 8(4), 70-83.

Talstra H., Uijttewaal W. S. J. and Stelling G. S., (2006), Emergence of large scale coherent structures in a shallow separating flow. Proceeding of the RiverFlow 2006 Conference, Lisbon, Portugal, Ferreira RML, Alves, ECTL, Leal JGAB and Cardosa AH (Eds), Taylor and Francis.

Task Force, (1963), Friction Factor in Open Channels. Report of the ASCE Task Force, J. Hydraul. Eng. ASCE, 89(2), 97-143.

Tukker J., (1997), Turbulence structures in shallow free-surface mixing layers. Ph.D. thesis, TU Delft.

Uijtewaal W. S. J and Booij R., (2000), Effects of shallowness on the development of free-surface mixing layers. Phys. of Fluids, 12(2), 392-420.

Van Prooijen B. C., (2004), Shallow mixing layers. Ph.D thesis, TU Delft.

White B. and Nepf H., (2007), Shear instability and coherent structures in a flow adjacent to a porous layer. J. Fluid Mech. 593, 1-32.

Wilcox D. C., (1994), Simulation of transition with a two-equation turbulence model. AIAA Journal, 32(2), 247-255.